JOURNAL OF APPLIED CRYSTALLOGRAPHY
ISSN 1600-5767

SGTools: a suite of tools for processing and analyzing large data sets from *in situ* X-ray scattering experiments

Nie Zhao,[a] Chunming Yang,[b,c,d]* Fenggang Bian,[b,c,d]* Daoyou Guo[e] and Xiaoping Ouyang[a]

[a]College of Materials Science and Engineering, Xiangtan University, Xiangtan, Hunan 411105, People's Republic of China, [b]Shanghai Synchrotron Radiation Facility, Shanghai Advanced Research Institute, Chinese Academy of Sciences, 239 Zhang Heng Road, Shanghai 201204, People's Republic of China, [c]Shanghai Institute of Applied Physics, Chinese Academy of Sciences, Shanghai 201800, People's Republic of China, [d]University of Chinese Academy of Sciences, Beijing 100049, People's Republic of China, and [e]Center for Optoelectronics Materials and Devices and Key Laboratory of Optical Field Manipulation of Zhejiang Province, Department of Physics, Zhejiang Sci-Tech University, Hangzhou, Zhejiang 310018, People's Republic of China. *Correspondence e-mail: yangchunming@zjlab.org.cn, bianfengggang@zjlab.org.cn

Received 21 January 2021
Accepted 18 November 2021

Edited by A. H. Liu, HPSTAR and Harbin Institute of Technology, People's Republic of China

Keywords: small-angle X-ray scattering; SAXS; grazing-incidence small-angle X-ray scattering; GISAXS; data processing; *in situ* experiments.

In situ synchrotron small-angle X-ray scattering (SAXS) is a powerful tool for studying dynamic processes during material preparation and application. The processing and analysis of large data sets generated from *in situ* X-ray scattering experiments are often tedious and time consuming. However, data processing software for *in situ* experiments is relatively rare, especially for grazing-incidence small-angle X-ray scattering (GISAXS). This article presents an open-source software suite (*SGTools*) to perform data processing and analysis for SAXS and GISAXS experiments. The processing modules in this software include (i) raw data calibration and background correction; (ii) data reduction by multiple methods; (iii) animation generation and intensity mapping for *in situ* X-ray scattering experiments; and (iv) further data analysis for the sample with an order degree and interface correlation. This article provides the main features and framework of *SGTools*. The workflow of the software is also elucidated to allow users to develop new features. Three examples are demonstrated to illustrate the use of *SGTools* for dealing with SAXS and GISAXS data. Finally, the limitations and future features of the software are also discussed.

1. Introduction

Small-angle X-ray scattering (SAXS) is a popular characterization technique in the research fields of biological macromolecules (Fratzl *et al.*, 1997; Blanchet & Svergun, 2013; Chakravarthy *et al.*, 2019), polymers (Vonk, 1973; Chu & Hsiao, 2001; Zhang *et al.*, 2018; Xiong *et al.*, 2018), colloidal solutions (Hashimoto *et al.*, 1998; Lassenberger *et al.*, 2017) and alloys (Williamson *et al.*, 1989; Dumont *et al.*, 2005; Kenel *et al.*, 2016) due to its easy sample preparation and provision of structural information averaged from a large sample area. Grazing-incidence small-angle X-ray scattering (GISAXS), a derivative method of SAXS, is also a powerful structural characterization technique for films (Renaud *et al.*, 2009; Lee *et al.*, 2005; Bhaway *et al.*, 2017). With the help of high-brilliance synchrotron radiation (SR) sources (Jaeschke *et al.*, 2016; Balerna & Mobilio, 2015), dynamic structure information on timescales of several milliseconds can be obtained by SR-SAXS, which is often used for *in situ* study during material preparation and application (Somani *et al.*, 2000; Polte *et al.*, 2010; Cravillon *et al.*, 2011).

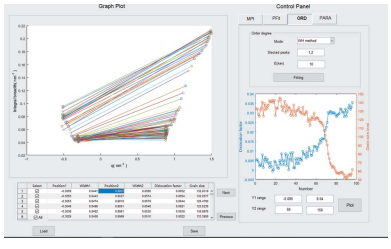

Table 1
Comparison of available data processing and analysis tools.

The 'features' column specifies the most important functions of the software. For example, software marked with a visualization function has a very complete data import, two-dimensional graph output with different formats, coordinate conversion, display in a three-dimensional style *etc*. Some software may have an incomplete visualization function, so this feature is not shown in the column. WAXS: wide-angle X-ray scattering; GISANS: grazing-incidence small-angle neutron scattering

Name	Programming language(s)	Open source	Online mode	Operating system(s)	Application	Features	Reference
SAXSutilities	MATLAB	GPL	Yes	Windows, Linux	SAXS	Online data processing and analysis	Sztucki & Narayanan (2007)
SasView	Python	GPL	NO	Windows, Linux,† Mac	SAXS	Data fitting and analysis	Alina *et al.* (2017)
BioXTAS RAW	Python	GPL	Yes	Windows, Linux, Mac	Biological SAXS	Data reduction and analysis	Nielsen *et al.* (2009)
FIT2D	Visual C	No	No	Windows	SAXS/GISAXS	Data reduction, analysis and visualization	Hammersley (2016)
Nika	Igor Pro	No	No	Windows, Mac	SAXS/WAXS, GISAXS	Data processing, reduction and visualization	Ilavsky (2012)
DPDAK	Python	GPL	Yes	Windows, Linux	SAXS	Large data set reduction and analysis	Benecke *et al.* (2014)
ATSAS	Fortran/C	No	No	Windows, Linux, Mac	Biological SAXS	Suite for data processing, fitting and analysis	Franke *et al.* (2017), Manalastas-Cantos *et al.* (2021)
PySAXS	Python	GPL	Yes	Windows, Linux, Mac	SAXS	Data processing and fitting	Taché *et al.* (2013)
FibreFix	C/Visual C	BSD	No	Windows	Fiber SAXS	Data processing, reduction and analysis, and visualization	Rajkumar *et al.* (2007)
GIXSGUI	MATLAB	No	No	Windows, Linux, Mac	GISAXS	Data reduction, visualization and indexing	Jiang (2015)
IsGISAXS	Fortran	No	No	Windows, Linux†	GISAXS	Simulation and fitting for nanoparticles	Lazzari (2002)
BornAgain	C++/Python	GPL	No	Windows, Linux,† Mac	GISAXS, GISANS	Simulation and fitting for multilayer architecture	Pospelov *et al.* (2020)
fitGISAXS	Igor Pro	No	No	Windows, Mac	GISAXS	Data reduction, fitting and analysis	Babonneau (2010)
HiPGISAXS	C++	No	No	Linux, Mac	GISAXS	Massively parallel high-performance simulation	Chourou *et al.* (2013)

To obtain structure information, data treatment such as coordinate system conversion, background correction, data reduction and model fitting is required. However, the processing of large data sets from *in situ* X-ray scattering experiments is typically tedious and time consuming. Thus, dedicated software tools are required for viewing, reduction and analysis of the recorded patterns.

There are several essential key features for fast and comprehensive data reduction and analysis software. (i) Complete modules including data processing and structure analysis, with a data format compatible with other software. (ii) Ease of use and automation for large data sets, especially for users without a programming background. (iii) Support for different operating systems including Windows, Linux and Mac. (iv) Powerful image and data processing ability, which could potentially save time when preparing publications.

Nowadays, several tools are available for SAXS and GISAXS data processing (Franke *et al.*, 2017; Hopkins *et al.*, 2017; Bressler *et al.*, 2015; Basham *et al.*, 2015; Jiang, 2015; Chourou *et al.*, 2013; Lazzari, 2002; Filik *et al.*, 2017; Kline, 2006; Abass *et al.*, 2017; Wright & Perkins, 2015; Breiby *et al.*, 2008; Shimizu *et al.*, 2016; Tate *et al.*, 2006; Hailey *et al.*, 2014; Hansen, 2014; Benecke *et al.*, 2014). Further details of some of these are given in Table 1.

The standalone program *FIT2D* (Hammersley, 2016) is flexible for data visualization and analysis, and is well known throughout the SAXS community. Large data sets can be processed through user-defined macro files, but it is not easily used by those with limited programming skills. In recent years, the powerful popular software *Nika* (Ilavsky, 2012) has been used to process data from CCD and other area detectors. It includes normalization, background correction, calibration and data integration modules, and several structure models have been implemented to obtain structure information through fitting to experimental data. The software *ATSAS* (Franke *et al.*, 2017; Manalastas-Cantos *et al.*, 2021) is a comprehensive suite for SAXS data analysis of biological macromolecules that can build a three-dimensional structure model for macromolecular complexes by combining SAXS, NMR and X-ray crystallography data. Similarly, the specialist software *FibreFix* (Rajkumar *et al.*, 2007) is designed to ascertain some important parameters of a fiber diffraction

pattern; information such as the pattern center, detector orientation and tilt angles can be estimated and refined. Data processing such as plotting putative unit cells over the scattering pattern, background subtraction and transformation of image space to reciprocal space can also be realized by the software.

Compared with the various software tools for SAXS data processing, tools for GISAXS data processing are relatively rare. The toolbox *GIXSGUI* (Jiang, 2015) is an efficient and simple-to-use software package that provides routine surface scattering data reduction methods. In addition, three-dimensional indexing is implemented to determine the space group and unit-cell parameters of nanostructures. The classic program *IsGISAXS* (Lazzari *et al.*, 2002) is powerful for simulation and analysis of GISAXS of islands supported on a substrate. It has been widely used for structural characterization of nanoparticle growth (Renaud *et al.*, 2003), self-assembly of block copolymers (Lee *et al.*, 2005) and quantum dots (Buljan *et al.*, 2012). Another software package, *FitGISAXS* (Babonneau, 2010), has also been developed for processing and modeling of GISAXS data based on the distorted-wave Born approximation. The simulation and fitting of models, such as monodisperse or polydisperse, and interacting particles with various size distributions, form factors and structure factors, could be realized. However, it is difficult to use to apply the models to the architecture of a multilayer film system. The recently developed software *BornAgain* (Pospelov *et al.*, 2020) provides a generic framework for the modeling of multilayer samples with smooth or rough interfaces and with various types of embedded nanoparticles. The structure model could be constructed through the graphical user interface. However, the simulation and fitting processes are usually time consuming due to the huge amount of calculation required. To speed up the computing process, the massively parallel X-ray data analysis code *HipGisaxs* (Chourou *et al.*, 2013) was developed, which is optimized for high efficiency with processor architectures on multi-core CPUs and NVidia GPUs. However, the preparation of reduced data for these GISAXS fitting software suites is also tedious and time consuming, especially when processing large data sets from *in situ* X-ray scattering experiments. Lastly in this overview, online software such as *DPDAK* (Benecke *et al.*, 2014) was developed for fast reduction and analysis of scanning SAXS data as well as GISAXS, which is useful for optimizing the experimental design effectively.

In this article, we present a new and open-source SAXS and GISAXS data analysis suite (*SGTools*) based on the MATLAB platform, which includes entire data processing modules for *in situ* X-ray scattering experiments. *SGTools* is now in use on the small-angle X-ray scattering beamline BL16B1 at the Shanghai Synchrotron Radiation Facility (Tian *et al.*, 2015; Li *et al.*, 2020). We present the main features of *SGTools*, and the framework and workflow are also elucidated to allow the user to develop new features. Finally, three examples demonstrate the use of *SGTools* for dealing with SAXS and GISAXS data. More descriptions of the tools can be found in the user document of the installed software.

2. Specifications and features

SGTools is a combined tool kit including multiple programs (*BP_Saxsview*, *Saxs_bg*, *Multi_plot*, *Format_TR*) which can be used to process SAXS and GISAXS data. These programs are written in MATLAB and made available as compiled packages, for which users do not require a MATLAB license. It is free and open source, available under the GNU General Public License (GPL version 3 or higher). The source code, install packages and full technical documentation for *SGTools* can be found at http://www.sgtools.cc. The software will be continuously updated to fix bugs and expand new functions.

The purpose of developing this software is to realize the treatment and analysis of large data sets obtained from *in situ* X-ray scattering experiments. The scattering data can be processed automatically through the online processing module, in which the program communicates directly with the detector system. The parameters for data processing are saved in a parameter file, which can be loaded into the tools to avoid the need to set parameters repeatedly. For the offline processing module, the developed toolkit contains programs for data calibration, two-dimensional scattering graph output, background correction, data integration, real-time animation generation (movie, GIF), time distribution of intensity curves (intensity mapping), several analysis modules, such as order degree analysis based on both a paracrystal model (Hosemann & Hindeleh, 1995) and Williamson–Hall (WH) theory (Lucks *et al.*, 2004), and interface correlation analysis for multilayer structure. Other tools including X-ray reflectivity data combination, file format transformation and penetration depth calculation are also implemented. For GISAXS setup, the scattering data are shown in the coordinate system of the scattering vector or scattering angle, where the incident angle can be automatically imported from the parameter file or the data file (specific name format). The scattering data can be integrated over a region of interest selected by the cursor, and the obtained data are shown in real time with the change in the selected region of interest. This is useful for researchers to determine a more appropriate region of interest in data processing and analysis.

3. Workflow and framework structure

The main flow of SAXS/GISAXS data processing is shown in Fig. 1: data import, data calibration, graph plotting, background (BG) subtraction, data reduction and data analysis. To realize the input of large data sets, *SGTools* includes both online and offline methods for importing raw data. For the online module, the program automatically synchronizes the file list with the data acquisition system. For the offline module, the user can manually add data files to the file list through the file browser, and the file list is saved in a matrix file to avoid importing data repeatedly in the subsequent data treatment. The user-friendly interface shown in Fig. 2 makes the program easy to use for those who do not have programming skills. The supported input formats for two-dimensional data are `*.tif` as used by the MAR-CCD and

Pilatus detectors, and other common formats like bitmap (`*.bmp`), eight-bit and 16-bit TIFF (`*.tif`), and PNG (`*.png`). The supported input data formats for one-dimensional data are columnar ASCII in *Excel* format (`*.csv`), *FIT2D* format (`*.chi`), raw data format (two columns without header information, `*.txt`) and the reduced data format used in *SGTools* (`*.sect`, `*.cake`). The output formats of composite images are standard graphic formats (`*.tif`, `*.bmp`, `*.jpg`, `*.pdf`, `*.eps`). In addition, the *Format_TR* tool is being developed to convert the 1D reduced data format between different software packages for data analysis. More information about the input and output file formats is provided in the user manual.

In the first step of the program, the data calibration module shown in Fig. 3 is used to determine the center position of the incident beam (beam center) and the sample-to-detector distance (SDD). The beam center is calculated via the standard circle equation by selecting several positions from the scattering ring. To improve the accuracy of the calculated value, the exact pixel positions of the selected scattering ring are refined by the profile of the scattering peaks (right-hand panel in Fig. 3). The SDD can then be calibrated using standard samples such as silver behenate and rat tendon. The equation for the SDD calibration is shown in equation (1*a*). The standard values of the scattering peaks are embedded within the program. After calibration, the instrument parameters are recorded for data processing and saved in the parameter file. The two-dimensional scattering pattern can then be plotted in the SAXS or GISAXS setup as shown in equations (1*b*)–(1*f*).

SDD calibration equation:

$$S_{\rm D} = \frac{P_{\rm st} - P_{\rm bc}}{\tan\left[\sin^{-1}(\lambda q_{\rm st}/4\pi)\right]}. \tag{1a}$$

SAXS mode:

$$q = \frac{4\pi}{\lambda}\sin(\theta). \tag{1b}$$

GISAXS mode:

$$q_x = k_0\left[\cos(2\theta_{\rm f})\cos(\alpha_{\rm f}) - \cos(\alpha_{\rm i})\right], \tag{1c}$$

$$q_y = k_0\left[\sin(2\theta_{\rm f})\cos(\alpha_{\rm f})\right], \tag{1d}$$

$$q_{||} = \left(q_x^2 + q_y^2\right)^{1/2}, \tag{1e}$$

$$q_{\perp} = k_0\left[\sin(\alpha_{\rm f}) + \sin(\alpha_{\rm i})\right]. \tag{1f}$$

$S_{\rm D}$ is the sample-to-detector distance, $q_{\rm st}$ is the standard value of the selected scattering peak for SDD calibration, $P_{\rm st}$ is the pixel position of the selected scattering peak, $P_{\rm bc}$ is the pixel position of the beam center and λ is the X-ray wavelength. In SAXS mode, q is the scattering vector amplitude and 2θ is the angle between the scattered and incident X-rays. In GISAXS mode, the scattering vector $\mathbf{q}$ is often decomposed into two components, $q_{||}$ and $q_{\perp}$. $k_0 = 2\pi/\lambda$ is the amplitude of the incident vector, $\alpha_{\rm i}$ is the incident angle, $\alpha_{\rm f}$ is the scattering angle with respect to the sample surface and $2\theta_{\rm f}$ is the in-plane angle with respect to the transmitted beam.

The background subtraction module can realize data correction of a two-dimensional scattering pattern or a one-

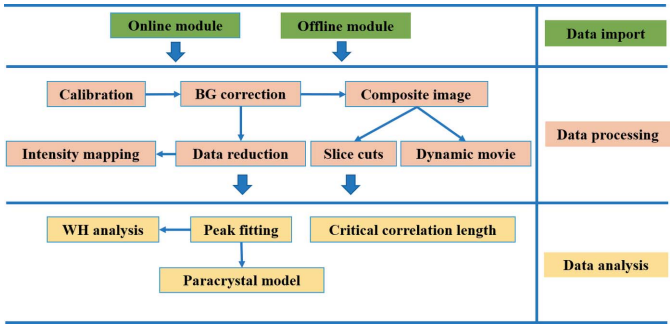

Figure 1
The main workflow and framework structure of *SGTools*.

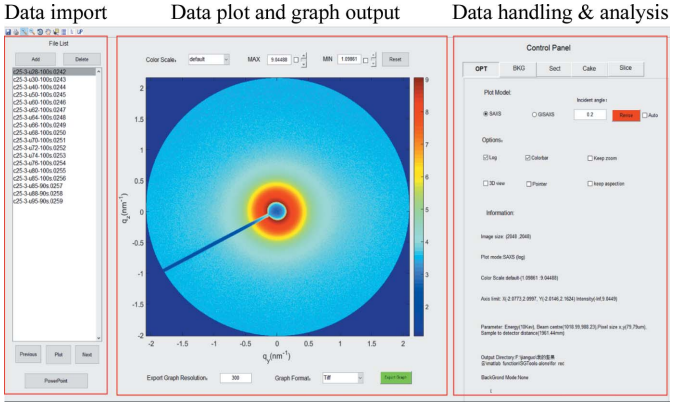

Figure 2
The interface of the main tool *BP_Saxsview* included in the *SGTools* suite. The interface of the tools is mainly divided into three regions: data import, data plot and graph output, and data reduction and analysis.

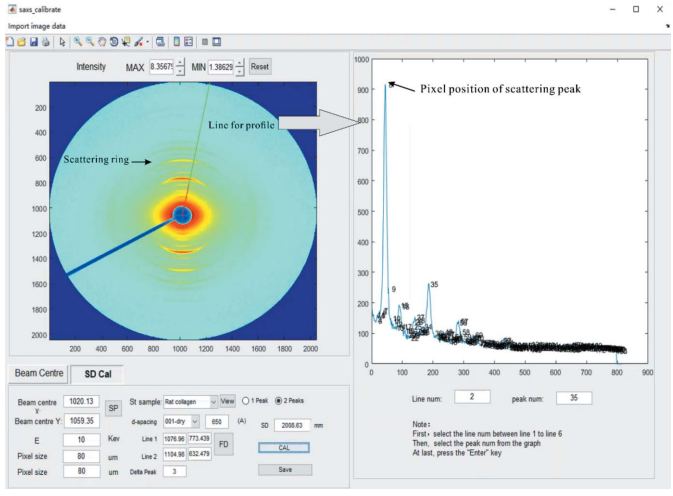

Figure 3
A screenshot of the data calibration module in *SGTools*. The beam center is determined by fitting the standard circle equation by selecting several positions from the scattering ring. The sample-to-detector distance is calibrated by the standard peak method.

dimensional intensity curve. According to the characteristics of the sample, it is divided into four cases as shown in equations (2*a*)–(2*d*) (Grishaev, 2012; Pauw, 2013).
Powder:

$$I_{\rm cor} = I_{\rm st} \exp\left[\frac{\mu t}{\cos(2\theta)}\right] - I_{\rm b}. \quad (2a)$$

Dilute solution:

$$I_{\rm cor} = I_{\rm st} \exp\left[\frac{\mu t}{\cos(2\theta)}\right] - c\, I_{\rm sov} - (1-c)\, I_{\rm b}. \quad (2b)$$

Concentrated solution:

$$I_{\rm cor} = I_{\rm st} \exp\left[\frac{\mu t}{\cos(2\theta)}\right] - I_{\rm sov}. \quad (2c)$$

Protein and nucleic acid solutions:

$$I_{\rm cor} = I_{\rm st} \exp\left[\frac{\mu t}{\cos(2\theta)}\right] - p\, I_{\rm sov}. \quad (2d)$$

Here, $I_{\rm cor}$ is the corrected scattering intensity, $I_{\rm st}$ is the sample scattering data collected by the detector, $I_{\rm b}$ is the scattering data of the blank sample, $I_{\rm sov}$ is the pure solvent scattering intensity of the solution sample, c is the volume fraction of the solvent in the sample, and p is the correction factor for protein and nucleic acid solutions. It can be approximately calculated as $1 - c_{\rm mg/ml} \times 7.4 \times 10^{-4}$ for proteins and $1 - c_{\rm mg/ml} \times 5.4 \times 10^{-4}$ for RNA/DNA, where $c_{\rm mg/ml}$ is the concentration of the sample. The absorption factor $\exp[-\mu t/\cos(2\theta)]$ represents the amount of absorption in the 2θ scattering direction after the scattered X-rays have penetrated through a sample of thickness t.

After background subtraction, the polarization correction function in *SGTools* can be applied to correct for the reduction in scattering intensity due to the polarization of the incident radiation. This is important to increase the accuracy of wide-angle scattering data. The correction factor for 2D detector images is given by Hura *et al.* (2000) as shown in equation (3),

$$I_{j,\rm cor} = I_j\Big(P_{\rm i}\{1 - [\sin(\psi)\sin(2\theta)]^2\} + (1-P_{\rm i})\{1 - [\cos(\psi)\sin(2\theta)]^2\}\Big), \quad (3)$$

where ψ is the azimuthal angle on the detector surface (defined here clockwise, 0 at 12 o'clock), 2θ is the scattering angle and $P_{\rm i}$ is the fraction of incident radiation polarized in the horizontal plane (azimuthal angle of 90°). The $P_{\rm i}$ factor of most synchrotron beamlines may be about 0.95 or so.

The data integrating module mainly includes methods of line, rectangular and arc integration, which can meet most data processing requirements. According to the type of symmetry, scattering patterns can be divided into isotropic scattering systems, rotational symmetry and specific orientation scattering systems. For isotropic scattering systems, the scattering intensity is symmetrical around the incident X-ray beam center; arc or sector integration is used to obtain the one-dimensional profile. For scattering systems with rotational symmetry, the commonly used data methods are polarization averaging or projection along the rotation axis. For scattering systems with a specific orientation, the available integration method is cutting of the selected region of interest, and this is commonly used for GISAXS data integration. The uncertainty of the reduced data is estimated by calculating the standard deviation of the processed data, which is useful for determining the error of the subsequent data analysis such as model fitting. In addition, a mask tool is provided to eliminate unwanted regions from the data processing, such as the module gap in the Pilatus detector, the X-ray beamstop and spurious data points. There are four types of region shape (ellipse, rectangle, polygon, freehand) for users to create the mask area in the image. The defined mask can be saved in a mask file (`*_mask.mat`) and loaded into the program directly.

The data analysis module has mainly been developed for the structural analysis of highly ordered systems such as ordered mesoporous films, nano-gratings and superlattices. The peak position and width of a scattering peak can be obtained by fitting peaks with the Gaussian–Lorenz blend function. A quantitative estimate of the order degree is then realized using the Williamson–Hall theory (Lucks *et al.*, 2004). The peak-fitting module can also be applied to the ordered structure analysis to develop a GISAXS model based on quasicrystal theory. The structure information of a film, including the nanostructure size, orientation, positional distribution factor, subunit number in the coherent region and length distribution of the nanostructure, can be obtained through fitting to the experimental data (Zhao *et al.*, 2014). The detail of these theories is described in the user manual. The slice-cuts module is used to analyze the critical correlation length, which is the characterization parameter of propagation effects between the interface and the surface of a thin film. When processing large data sets, the batch-processing module can be defined according to the characteristics of the research system. Parallel computing utilizing the features of graphics and multicore processors is intended to be implemented in the future.

4. Results and application examples

To give an introduction to the capabilities of *SGTools*, we present three examples of data processing and analysis using the developed software. In the first example, an *in situ* SAXS experiment was conducted to monitor the sol–gel transition during heating. The composite images after background correction were created using the *BP_Saxsview* tool (Fig. 4). To show the weak peaks, high dynamic range imaging is used to increase the contrast between the scattering peaks and background. As shown in the patterns, no scattering peaks were found at room temperature, indicating the disordered structure of the sol. As the temperature was gradually increased, a weak scattering ring was observed which corresponds to the transition from disordered sol to ordered gel. A reversible transition from ordered gel to disordered sol was also observed as the temperature was gradually decreased to

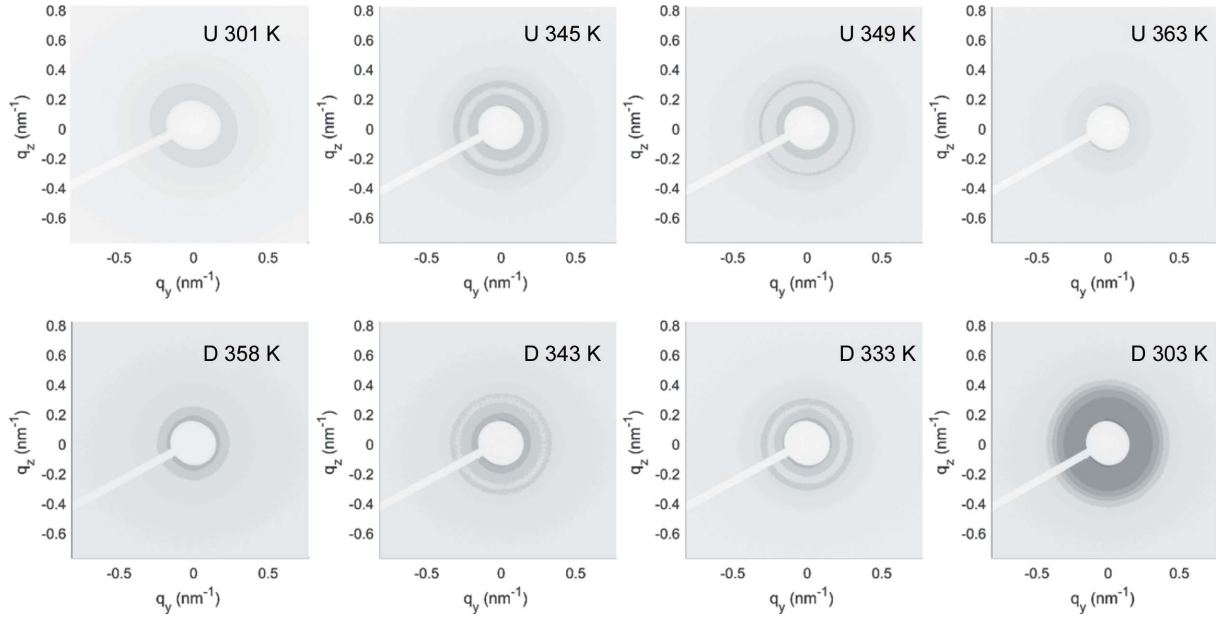

Figure 4
2D SAXS scattering patterns of the gel during the sol–gel transition induced by varying the temperature. U and D represent the heating and cooling processes, respectively.

room temperature. To analyze the sol–gel transition process quantitatively, the data reduction module was used to integrate the scattering patterns into one-dimensional profiles. The intensity mapping as a function of the frame number was plotted by the *multi_3D_plot* module as shown in Fig. 5.

As the critical temperature of the sol–gel transition was approached, the ordered structure was shown to form quickly, within just a few minutes. In addition, the period of the ordered structure decreased gradually with increasing temperature up to 358 K, which is indicated by the increased q value of the scattering peak. Interestingly, the ordered structure reappeared and then disappeared again as the temperature decreased from 363 to 303 K. Therefore, the mapping of the intensity distribution $I(q)$ with annealing time is a useful tool for studying the dynamic mechanism of the sol–gel transition, for which the details of the transition process can be effectively obtained.

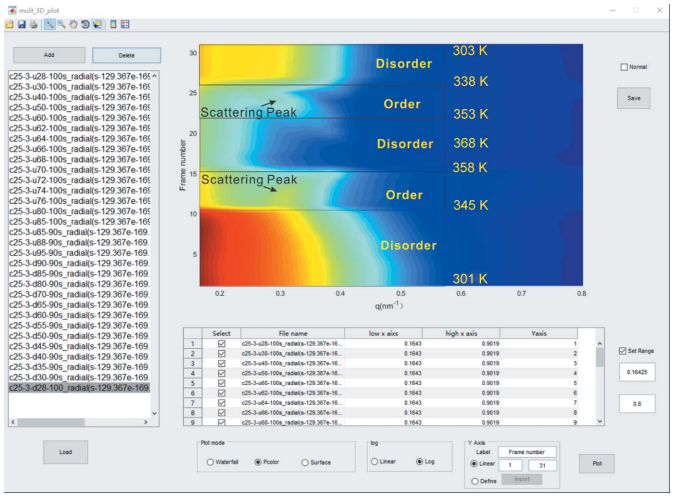

Figure 5
Intensity mapping as a function of the frame number as plotted by the *multi_3D_plot* module. The structure transition from disorder to order is determined by the appearance and disappearance of the scattering peaks. The scattering peaks are labeled by arrows.

A polyelectrolyte multilayer (PEM) was prepared by the layer-by-layer technique through alternating adsorption of oppositely charged polyions onto a charged surface. Such multilayers have potential applications in optical devices, sensing, drug release and biologically active coatings. During the layer-by-layer self-assembly process, the surface microstructure is partially propagated from the interface between the polyelectrolyte films and the substrate.

As shown in Fig. 6(*a*), intense resonant diffuse scattering was detected in a PEM film with ten bilayers, as indicated by intensity modulation between the Yoneda and reflected beam. The resonant diffusion was gradually weakened with increasing numbers of bilayers of PEM film. This indicates that the correlation between the interface and the surface was lost at small in-plane length scales. The intensity profiles of the modulations were obtained using the slice module of *SGTools*, as shown in Fig. 6(*c*). The slice region is defined by the coordinates of the lower left and upper right for the cursor-selected rectangle. The slice steps and width are used to adjust the number and width of line integrals within the region. A critical lateral cutoff length R_c to estimate the smallest lateral structure length replicated between the interface and the surface was determined by the equation $R_c = 2\pi/\Delta q_{coor}$, where Δq_{coor} is the lateral (along q_y) propagation length of the modulation in reciprocal space (Müller-Buschbaum & Stamm, 1998), which was determined through the amplitude of the modulations decreasing with increasing q_y. The R_c values of PEM films with ten and 12 bilayers were estimated to be 94.5 and 131.8 nm, respectively. This means that the profile of the

structure was propagated from the interface, where structure smaller than the critical length was gradually lost. A detailed description can be found in our previous study (Zhao *et al.*, 2016).

The *Bat-pro* function was developed to realize batch data processing. This function can automatically load and process multiple data imported from a file list. This is useful for researchers to treat large data sets in time-resolved X-ray scattering experiments with high efficiency. Detailed instructions about how to use the batch-processing function are provided in the user manual.

In our last example, the dynamic structure evolution of an ordered mesoporous film during template removal was monitored by *in situ* GISAXS investigation. As shown in Fig. 7, sections of the scattering patterns were analyzed as a function of annealing time. The scattering peaks (labeled by circles) show a complex variation in the vertical direction. An initial 2D hexagonal structure with *p6mm* (vector angle 30°) symmetry was distorted to a *c2mm* (vector angle 45°) plane group due to this uniaxial shrinkage. This means that significant shrinkage in the framework has been observed after template removal, resulting in a decrease in the quality of the ordered structure.

To study the dynamic structure evolution quantitively, the 11 scattering peak is fitted to the Gaussian–Lorentz blend equation as shown in equation (4),

$$I(q) = m \exp\left[-\frac{-(q-q_z)^2}{2w^2}\right] + (1-m)\,\frac{w^2}{w^2 + 4(q-q_z)^2}. \tag{4}$$

Here, m represents Gaussian character in the blend function. The fitting function developed by O'Haver (2008) was embedded into the *PFit* module to obtain peak information, including peak position, peak height, peak area and peak width (Fig. 8). Details of the fitting function are provided in the user manual. The q_z position and peak width w were obtained as a function of calcination time, as shown in Fig. 9. The fast change in the peak position and peak width indicates structure variation within the mesoporous film (Zhao *et al.*, 2019).

According to the Williamson–Hall theory, peak width broadening can be divided into strain (mesochannel dislocation) and size (grain size) components. Strain broadening usually increases with decreasing order of the scattering peaks, but peak broadening is order independent. The factors of mesochannel dislocation and grain size were refined by fitting the peak position and peak width to the Williamson–Hall equation:

$$\beta_i^* \equiv \frac{\beta_i \cos(\theta_i)}{\lambda} = \frac{2\pi}{D_V} + 2\varepsilon q_i. \tag{5}$$

Here, β_i^* is the integral breadth of the total broadening in reciprocal space, q_i is the position for the peak being considered, D_V is the volume-weighted grain size and ε is the dislocation factor for the measurement of microstrain.

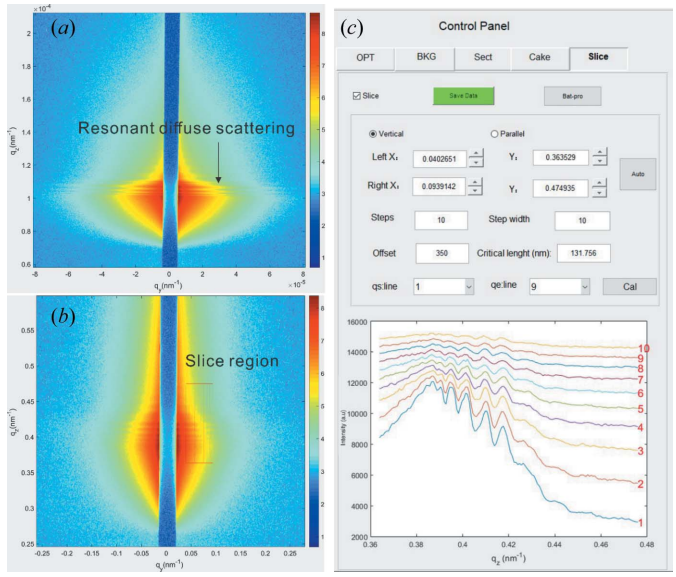

Figure 6
Analysis of the partial roughness propagation effect for PEM films. (*a*) A GISAXS pattern for a PEM film with ten bilayers. Strong resonant diffuse scattering is indicated by the arrow. (*b*) A GISAXS pattern for a PEM film with 12 bilayers. The slice region for critical length analysis is indicated by the rectangle. (*c*) Vertical cuts from the 2D pattern [slice region in panel (*b*)] at different q_y positions are plotted against q_z. For clarity, the curves are shifted vertically without maintaining the scale. The modulation decreases as q_y increases and disappears at $q_y = q_{coor}$ [labeled with red numerals from 1 to 10 in the bottom right of panel (*c*)].

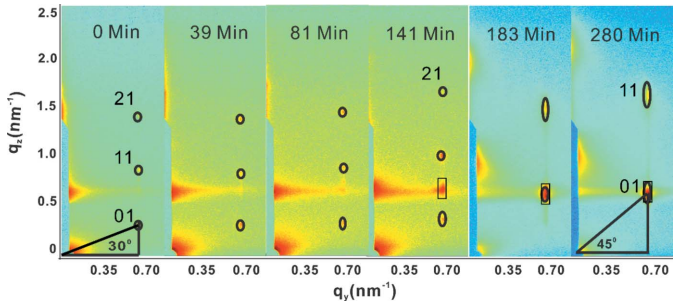

Figure 7
GISAXS analysis of the mesoporous film during the template removal process with a heating rate of 3 K min^{-1}.

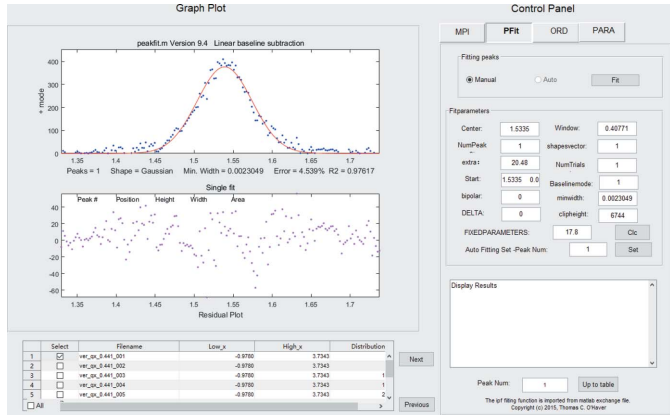

Figure 8
The interface of the *PFIT* module in *SGTools*.

According to equation (5), there should be a linear relationship between β_i^* and q_i, and the values of D_V and the dislocation factor ε can then be directly estimated from the intercept and slope of the straight line, respectively. The MATLAB routine *polyfit* with the degree of polynomial fit n = 1 was then used to fit the data to obtain the structure parameters of the dislocation factor and grain size as shown in Fig. 10. The root-mean-square error (RMSE) and coefficient of determination R can be used to estimate the uncertainty of the fitting results. However, the large data sets typically produced by *in situ* X-ray scattering experiments are commonly tedious to handle. To increase the processing efficiency, the peak information obtained from the *PFit* fitting function is automatically recorded in a table (lower left panel in Fig. 10). The Williamson–Hall analysis module then batch fits the data sets in the table. The structure information obtained from the fitting results is plotted as a function of annealing time, as shown in the right-hand panel of Fig. 10.

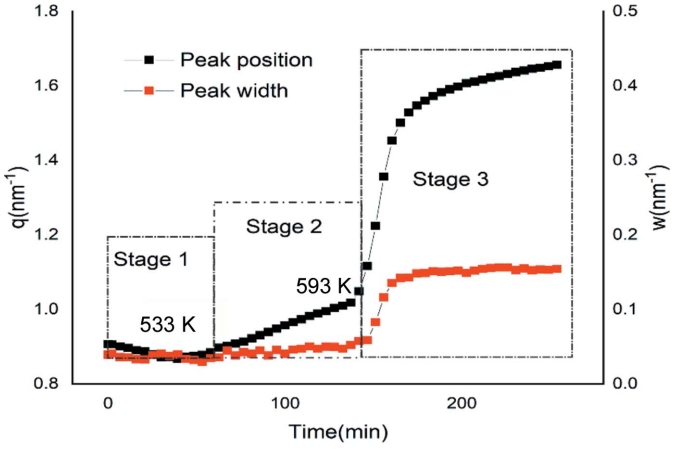

Figure 9
The q_z position and width of the 11 peak as a function of calcination time. The calcination process is divided into three stages, with stage transition temperatures of 533 and 593 K.

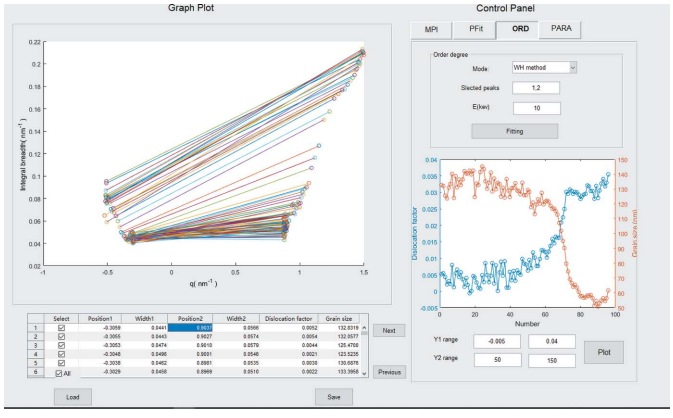

Figure 10
The user interface of the order degree analysis module included in *SGTools*.

5. Conclusions and outlook

The *in situ* SAXS technique is a powerful tool for studying the dynamic structures and mechanisms of materials during preparation and application processes. The developed software contains tools for data import, data calibration, background subtraction, integral processing and data analysis. The scattering data can be reduced dynamically over a region of interest selected by the cursor, and the results are plotted in real time with changes in the selected region of interest. Some specific functions for *in situ* X-ray scattering experiments, such as mapping of intensity cuts, composite images and real-time movies, have been developed and are included in the current tools. The analysis module is used to estimate quantitively the structure order degree in ordered systems.

The target of the *SGTools* package is the processing and analysis of large data sets from *in situ* X-ray scattering experiments. The basic functions are optimized according to the features of several dynamic processes in the current version, such as template removal of a highly ordered mesoporous film. In the future, the inclusion of modules for additional specific *in situ* X-ray scattering experiments, such as fiber stretching processes and charging and discharging processes of batteries, and the construction of three-dimensional reciprocal images are envisaged. In addition, parallel computing by GPU and multicore processors should be implemented to accelerate the data processing. The open-source code allows the user to integrate new features directly into the tools for personalized application.

Funding information

Funding for this research was provided by: National Natural Science Foundation of China (grant No. 12175295; grant No. 12027813; grant No. U1932118; grant No. 11605149); Natural Science Foundation of Hunan Province (grant No. 2020JJ4086); Education Department of Hunan Province (grant No. 19B570); China Postdoctoral Science Foundation (grant No. 2017M622595); Zhejiang Public Service Technology Research Program (award No. LGC19F040001); National Key Research and Development Program of China (award No. 2017YFA0403000); Science and Technology Commission of Shanghai Municipality (award No. 17JC1400802).

References

Abass, A., Bell, J. S., Spang, A., Hayes, S., Meek, K. M. & Boote, C. (2017). *J. Appl. Cryst.* **50**, 1235–1240.
Alina, G., Butler, P., Cho, J., Doucet, M. & Kienzle, P. (2017). *SasView for Small Angle Scattering Analysis*, http://www.sasview.org.
Babonneau, D. (2010). *J. Appl. Cryst.* **43**, 929–936.
Balerna, A. & Mobilio, S. (2015). *Synchrotron Radiation: Basics, Methods and Applications*, edited by S. Mobilio, F. Boscherini & C. Meneghini, ch. 1, pp. 3–28. Heidelberg: Springer.
Basham, M., Filik, J., Wharmby, M. T., Chang, P. C. Y., El Kassaby, B., Gerring, M., Aishima, J., Levik, K., Pulford, B. C. A., Sikharulidze, I., Sneddon, D., Webber, M., Dhesi, S. S., Maccherozzi, F., Svensson, O., Brockhauser, S., Náray, G. & Ashton, A. W. (2015). *J. Synchrotron Rad.* **22**, 853–858.
Benecke, G., Wagermaier, W., Li, C., Schwartzkopf, M., Flucke, G., Hoerth, R., Zizak, I., Burghammer, M., Metwalli, E., Müller-

Buschbaum, P., Trebbin, M., Förster, S., Paris, O., Roth, S. V. & Fratzl, P. (2014). *J. Appl. Cryst.* **47**, 1797–1803.
Bhaway, S. M., Qiang, Z., Xia, Y., Xia, X., Lee, B., Yager, K. G., Zhang, L., Kisslinger, K., Chen, Y.-M., Liu, K., Zhu, Y. & Vogt, B. D. (2017). *ACS Nano*, **11**, 1443–1454.
Blanchet, C. E. & Svergun, D. I. (2013). *Annu. Rev. Phys. Chem.* **64**, 37–54.
Breiby, D. W., Bunk, O., Andreasen, J. W., Lemke, H. T. & Nielsen, M. M. (2008). *J. Appl. Cryst.* **41**, 262–271.
Bressler, I., Pauw, B. R. & Thünemann, A. F. (2015). *J. Appl. Cryst.* **48**, 962–969.
Buljan, M., Radić, N., Bernstorff, S., Dražić, G., Bogdanović-Radović, I. & Holý, V. (2012). *Acta Cryst.* A**68**, 124–138.
Chakravarthy, S., Hopkins, J., Bilsel, O. & Irving, T. (2019). *FASEB J.* **33**, 779.
Chourou, S. T., Sarje, A., Li, X. S., Chan, E. R. & Hexemer, A. (2013). *J. Appl. Cryst.* **46**, 1781–1795.
Chu, B. & Hsiao, B. S. (2001). *Chem. Rev.* **101**, 1727–1762.
Cravillon, J., Schröder, C. A., Nayuk, R., Gummel, J., Huber, K. & Wiebcke, M. (2011). *Angew. Chem. Int. Ed.* **50**, 8067–8071.
Dumont, M., Lefebvre, W., Doisneau-Cottignies, B. & Deschamps, A. (2005). *Acta Mater.* **53**, 2881–2892.
Filik, J., Ashton, A. W., Chang, P. C. Y., Chater, P. A., Day, S. J., Drakopoulos, M., Gerring, M. W., Hart, M. L., Magdysyuk, O. V., Michalik, S., Smith, A., Tang, C. C., Terrill, N. J., Wharmby, M. T. & Wilhelm, H. (2017). *J. Appl. Cryst.* **50**, 959–966.
Franke, D., Petoukhov, M. V., Konarev, P. V., Panjkovich, A., Tuukkanen, A., Mertens, H. D. T., Kikhney, A. G., Hajizadeh, N. R., Franklin, J. M., Jeffries, C. M. & Svergun, D. I. (2017). *J. Appl. Cryst.* **50**, 1212–1225.
Fratzl, P., Jakob, H. F., Rinnerthaler, S., Roschger, P. & Klaushofer, K. (1997). *J. Appl. Cryst.* **30**, 765–769.
Grishaev, A. (2012). *Curr. Protoc. Protein Sci.* **70**, 17.
Hailey, A. K., Hiszpanski, A. M., Smilgies, D.-M. & Loo, Y.-L. (2014). *J. Appl. Cryst.* **47**, 2090–2099.
Hammersley, A. P. (2016). *J. Appl. Cryst.* **49**, 646–652.
Hansen, S. (2014). *J. Appl. Cryst.* **47**, 1469–1471.
Hashimoto, T., Saijo, K., Harada, M. & Toshima, N. (1998). *J. Chem. Phys.* **109**, 5627–5638.
Hopkins, J. B., Gillilan, R. E. & Skou, S. (2017). *J. Appl. Cryst.* **50**, 1545–1553.
Hosemann, R. & Hindeleh, A. (1995). *J. Macromol. Sci. Part B*, **34**, 327–356.
Hura, G., Sorenson, J. M., Glaeser, R. M. & Head-Gordon, T. (2000). *J. Chem. Phys.* **113**, 9140–9148.
Ilavsky, J. (2012). *J. Appl. Cryst.* **45**, 324–328.
Jaeschke, E. J., Khan, S., Schneider, J. R. & Hastings, J. B. (2016). Editors. *Synchrotron Light Sources and Free-Electron Lasers: Accelerator Physics, Instrumentation and Science Applications.* Heidelberg: Springer.
Jiang, Z. (2015). *J. Appl. Cryst.* **48**, 917–926.
Kenel, C., Schloth, P., Van Petegem, S., Fife, J., Grolimund, D., Menzel, A., Van Swygenhoven, H. & Leinenbach, C. (2016). *JOM*, **68**, 978–984.
Kline, S. R. (2006). *J. Appl. Cryst.* **39**, 895–900.
Lassenberger, A., Grünewald, T., van Oostrum, P., Rennhofer, H., Amenitsch, H., Zirbs, R., Lichtenegger, H. & Reimhult, E. (2017). *Chem. Mater.* **29**, 4511–4522.
Lazzari, R. (2002). *J. Appl. Cryst.* **35**, 406–421.
Lee, B., Park, I., Yoon, J., Park, S., Kim, J., Kim, K.-W., Chang, T. & Ree, M. (2005). *Macromolecules*, **38**, 4311–4323.
Li, Y.-W., Liu, G.-F., Wu, H.-J., Zhou, P., Hong, C-X., Li, N. & Bian, F.-G. (2020). *Nucl. Sci. Tech.* **31**, 117.
Lucks, I., Lamparter, P. & Mittemeijer, E. J. (2004). *J. Appl. Cryst.* **37**, 300–311.
Manalastas-Cantos, K., Konarev, P. V., Hajizadeh, N. R., Kikhney, A. G., Petoukhov, M. V., Molodenskiy, D. S., Panjkovich, A., Mertens, H. D. T., Gruzinov, A., Borges, C., Jeffries, C. M., Svergun, D. I. & Franke, D. (2021). *J. Appl. Cryst.* **54**, 343–355.
Müller-Buschbaum, P. & Stamm, M. (1998). *Macromolecules*, **31**, 3686–3692.
Nielsen, S. S., Toft, K. N., Snakenborg, D., Jeppesen, M. G., Jacobsen, J. K., Vestergaard, B., Kutter, J. P. & Arleth, L. (2009). *J. Appl. Cryst.* **42**, 959–964.
O'Haver, T. C. (2008). *Matlab/Octave Peak Fitters*, https://terpconnect.umd.edu/~toh/spectrum/InteractivePeakFitter.htm.
Pauw, B. R. (2013). *J. Phys. Condens. Matter*, **25**, 383201.
Polte, J., Erler, R., Thünemann, A. F., Sokolov, S., Ahner, T. T., Rademann, K., Emmerling, F. & Kraehnert, R. (2010). *ACS Nano*, **4**, 1076–1082.
Pospelov, G., Van Herck, W., Burle, J., Carmona Loaiza, J. M., Durniak, C., Fisher, J. M., Ganeva, M., Yurov, D. & Wuttke, J. (2020). *J. Appl. Cryst.* **53**, 262–276.
Rajkumar, G., AL-Khayat, H. A., Eakins, F., Knupp, C. & Squire, J. M. (2007). *J. Appl. Cryst.* **40**, 178–184.
Renaud, G., Lazzari, R. & Leroy, F. (2009). *Surf. Sci. Rep.* **64**, 255–380.
Renaud, G., Lazzari, R., Revenant, C., Barbier, A., Noblet, M., Ulrich, O., Leroy, F., Jupille, J., Borensztein, Y., Henry, C. R., Deville, J. P., Scheurer, F., Mane-Mane, J. & Fruchart, O. (2003). *Science*, **300**, 1416–1419.
Shimizu, N., Yatabe, K., Nagatani, Y., Saijyo, S., Kosuge, T. & Igarashi, N. (2016). *AIP Conf. Proc.* **1741**, 050017.
Somani, R. H., Hsiao, B. S., Nogales, A., Srinivas, S., Tsou, A. H., Sics, I., Balta-Calleja, F. J. & Ezquerra, T. A. (2000). *Macromolecules*, **33**, 9385–9394.
Sztucki, M. & Narayanan, T. (2007). *J. Appl. Cryst.* **40**, s459–s462.
Taché, O., Spalla, O., Thill, A. & Sen, D. (2013). *pySAXS, an Open Source Python Package and GUI for SAXS Data Treatment*, https://iramis.cea.fr/en/Phocea/Vie_des_labos/Ast/ast_sstechnique.php?id_ast=1799.
Tate, M. P., Urade, V. N., Kowalski, J. D., Wei, T., Hamilton, B. D., Eggiman, B. W. & Hillhouse, H. W. (2006). *J. Phys. Chem. B*, **110**, 9882–9892.
Tian, F., Li, X., Wang, Y., Yang, C., Zhou, P., Lin, J., Zeng, J., Hong, C., Hua, W., Li, X., Miao, X., Bian, F. & Wang, J. (2015). *Nucl. Sci. Tech.* **26**, 030101.
Vonk, C. G. (1973). *J. Appl. Cryst.* **6**, 81–86.
Williamson, D. L., Mahan, A., Nelson, B. & Crandall, R. (1989). *Appl. Phys. Lett.* **55**, 783–785.
Wright, D. W. & Perkins, S. J. (2015). *J. Appl. Cryst.* **48**, 953–961.
Xiong, B., Chen, R., Zeng, F., Kang, J. & Men, Y. (2018). *J. Membr. Sci.* **545**, 213–220.
Zhang, Q., Li, L., Su, F., Ji, Y., Ali, S., Zhao, H., Meng, L. & Li, L. (2018). *Macromolecules*, **51**, 4350–4362.
Zhao, N., Hua, W., Wang, Y., Yang, C., Ouyang, X., Yuan, B. & Bian, F. (2019). *Appl. Surf. Sci.* **479**, 776–785.
Zhao, N., Yang, C., Wang, Y., Zhao, B., Bian, F., Li, X. & Wang, J. (2016). *Mater. Sci. Eng. C*, **58**, 352–358.
Zhao, N., Yang, C., Zhang, Q., Lu, X., Wang, Y. & Wang, J. (2014). *J. Appl. Phys.* **115**, 204311.